MULTISCALE MODEL. SIMUL.
Vol. 16, No. 1, pp. 106–124

NETWORK MODELING OF FLUID TRANSPORT THROUGH SEA ICE WITH ENTRAINED EXOPOLYMERIC SUBSTANCES*

KYLE R. STEFFEN†, YEKATERINA EPSHTEYN†, JINGYI ZHU†, MEGAN J. BOWLER†, JODY W. DEMING‡, AND KENNETH M. GOLDEN†

Abstract. Sea ice hosts a rich ecosystem of flora and fauna, from microscale to macroscale. Algae living in its porous brine microstructure, such as the diatom *Melosira arctica*, secrete gelatinous exopolymeric substances (EPS) which are thought to protect these communities from their cold and highly saline environment. Recent experimental work has shown significant changes in the structure and properties of young sea ice with entrained *Melosira* EPS, such as increased brine volume fraction, salt retention, pore tortuosity, and decreased fluid permeability. In particular, we find that the cross-sectional areas of the brine inclusions are described by a bimodal–lognormal distribution, which generalizes the classic lognormal distribution of Perovich and Gow. We propose a model for the effective fluid permeability of young, EPS-laden sea ice, consisting of a random network of pipes with cross-sectional areas chosen from this bimodal distribution. We consider an equilibrium model posed on a square lattice, incorporating only the most basic features of the geometry and connectivity of the brine microstructure, and find good agreement between our model and the observed drop in fluid permeability. Our model formulation suggests future directions for experimental work, focused on measuring the inclusion size distribution and fluid permeability of sea ice with entrained EPS as functions of brine volume fraction. The drop in fluid permeability observed in experimental work and predicted by the model is significant, and should be taken into account, for example, in physical or ecological process models involving fluid or nutrient transport.

Key words. sea ice, porous media, fluid permeability, exopolymeric substances, network model

AMS subject classifications. 00A69, 76S05, 90B15

DOI. 10.1137/17M1117513

1. Introduction.

Sea ice that forms on the surface of high latitude oceans hosts a rich ecosystem, from autotrophs (algae) and other microorganisms that dwell within the ice, to small crustaceans that feed below it (e.g., krill), and the macrofauna that forage from it (e.g., penguins or polar bears in the Southern or Northern hemispheres, respectively). Indeed, the higher trophic levels of current polar ecosystems largely depend on sea ice as a platform on which to live, forage, and reproduce [40]. The areal extent and physical properties of sea ice also figure significantly in global climate models [17]. The growth, structure, and properties of ice formed from seawater containing the major ions (Na^+, K^+, Ca^{2+}, Cl^-, ${SO_4}^{2-}$, ${CO_3}^{2-}$) have been studied for decades [30, 40, 43, 44]. On the macroscale, much of what is known comes from remote sensing of sea ice via airborne platforms such as satellites, planes, and helicopters [4, 5, 12, 15, 24], as well as expeditions into Earth's sea ice packs [25, 26, 28, 29, 34]. On the microscale, much has been learned from analysis of both natural sea ice [27, 30, 40] as well as artificially grown sea ice, which is generally devoid of life and its organic products [13, 18, 30, 40]. In broad strokes, we can say that sea ice is a porous medium

*Received by the editors February 21, 2017; accepted for publication (in revised form) September 21, 2017; published electronically January 11, 2018.
http://www.siam.org/journals/mms/16-1/M111751.html
Funding: This work was funded by the National Science Foundation through grants DMS-0602219, ARC-0934721, DMS-0940249, and DMS-1413454, and the Office of Naval Research through grant N00014-13-10291. The fifth author was funded by the Karl M. Banse Endowed Professorship.
†Department of Mathematics, University of Utah, Salt Lake City, UT 84112 (steffen@math.utah.edu, epshteyn@math.utah.edu, zhu@math.utah.edu, megan.j.bowler@gmail.com, golden@math.utah.edu).
‡School of Oceanography, University of Washington, Seattle, WA 98195 (jdeming@uw.edu).

exhibiting structure over many length scales, principally composed of a solid matrix of pure ice, with inclusions of brine (including microorganisms and their exudates), salt, air, and other impurities. Moreover, the microstructure of sea ice evolves with time, as fluid flowing through the porous microstructure tends to modify inclusion connectivity and channel structure.

The effect of algae or their cell-free organic matter on the growth, structure, and properties of sea ice is not as well understood. Recent work of Krembs, Eicken, and Deming [23] compared artificial sea ice grown from seawater containing exopolymeric substances (EPS) with several controls, and observed that the artificial EPS-laden ice had a more tortuous microstructure, larger brine volume fraction, greater salt retention, and a net drop in fluid permeability. In sea ice, larger volume fractions and larger salinities typically lead to larger fluid permeabilities. On the other hand, scaling considerations for general porous media indicate that fluid permeability decreases with the square of tortuosity [7]. As proposed in [23], one possible explanation for the observed net drop in fluid permeability is that the observed increases in brine volume fraction and salt retention were not enough to overcome the observed increase in tortuosity.

Models of fluid flow through porous media, and fluid flow through sea ice, vary widely in complexity. General studies (unrelated to sea ice) include Koplik [21], who posed a network (pipe) model for linear Stokes flow in a regular periodic network; Koplik, Lin, and Vermette [22], who applied the network model of [21] to porous media, in particular Massillon sandstone; Torquato and Pham [42], who derived "void bounds" on the fluid permeability of hierarchical porous media, including coated parallel, circular pipe geometries; and Hyman, Smolarkiewicz, and Winter [19], who numerically integrated the Navier–Stokes equations in the pore space of a stochastically generated porous medium, and studied the heterogeneities of flow. Studies specific to sea ice include [11, 13, 14, 45] (the latter two to be described below).

Zhu et al. [45] posed and analyzed a model for fluid flow through sea ice consisting of a random network of pipes, followed by small but important modifications in [13]. While the model is a two-dimensional pipe network based on a square lattice, and assumes a given equilibrium state, the effective fluid permeability of the pipe network agreed well with the data of Freitag [9] for the fluid permeability of artificially grown, young sea ice.

In this work, we extend the two-dimensional model of [13, 45], based on the findings in [23], to consider the effects of microscale biochemistry in young sea ice, in particular the presence of algal exudates, on the larger scale fluid transport properties of the ice. In the remainder of this introductory section, we summarize the original random network (pipe) model of [13, 45], and recall the void bounds of [14, 42] for fluid transport in sea ice; in section 2, we conclude the discussion of the original model, including all the details such as parameter selection; in section 3, we develop our new model and state the main results; and we conclude in section 4.

1.1. Random network model for fluid transport through sea ice. In this section, we recall the random pipe network model of [45], including a synopsis of the derivations of the linear system and the effective parameter k.

Consider a vertical slab of sea ice, with a given brine volume fraction $\phi \in [0, 1)$, and given dimensions $L \times D \times h$ m^3, where D is the vertical depth, L the horizontal span, and h the horizontal thickness. Note that $h \ll D, L$ can be viewed as the dimension of a cell in which a typical brine inclusion is contained. Moreover, note that h is assumed to be related to D and L, which will be clarified in the following

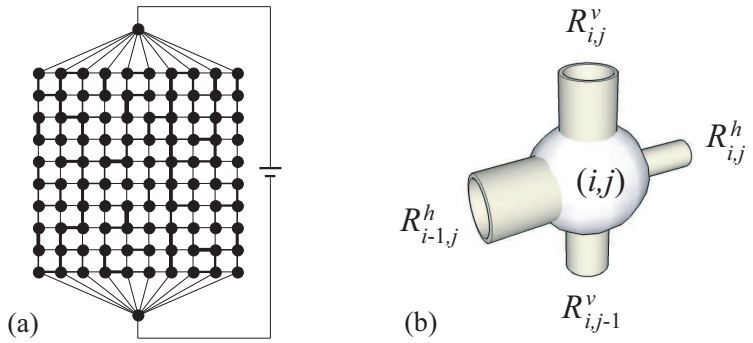

FIG. 1. *From* [45] *(reprinted from the Annals of Glaciology with permission of the International Glaciological Society):* (a) *a depiction of a random pipe network on a square lattice; and* (b) *a close-up view of the* (i,j)*th node, and the adjoining circular pipes with randomly distributed radii.*

paragraph. The random pipe network model is formulated as follows.

Consider a square lattice

$$\mathbb{L} = \{(hi, hj) \in \mathbb{R}^2 : 0 \le i \le m, 0 \le j \le n\}, \tag{1}$$

where $h = L/m = D/n$ for some given $m, n \in \mathbb{Z}$. The parameter h can be viewed as the size of a typical brine inclusion. We form a random pipe network from $\mathbb{L}$ by connecting a given node (i,j) (shorthand for the node located at the point (hi, hj)) to its four nearest neighbors $\{(i \pm 1, j), (i, j \pm 1)\}$ with fluid filled pipes, and choose the cross-sectional area of each pipe from a random distribution A comparable to the brine inclusions found in young sea ice. Next, induce an upward flow through the network by a pressure drop $p_b - p_t$, where $p_b > p_t$ are the pressures at the bottom and top of the network, respectively; see Figure 1.

Denote $R^v_{i,j}$ and $R^h_{i,j}$ as the radii of the pipes connecting the nodes with indices $(i,j), (i,j+1)$ and $(i,j), (i+1,j)$, respectively. (Similarly, denote $A^v_{i,j}$ and $A^h_{i,j}$ as the cross-sectional area of these pipes.) For each pipe of radius R, the fluid flow within is assumed to be a classic Poiseuille flow, with flux Q given by

$$Q = -\frac{\pi R^4}{8\mu} \nabla \mathcal{P}, \tag{2}$$

where $\nabla \mathcal{P}$ is the constant pressure gradient in the pipe, and μ is the fluid viscosity. Let $p_{i,j}$ denote the pressure in the fluid at the (i,j)th node of the network; since the pipe length h is small, in [45] the pressure gradient $\nabla \mathcal{P}$ is approximated by a standard finite difference:

$$\nabla \mathcal{P} \approx \frac{p_{i+1,j} - p_{i,j}}{h} \quad \text{or} \quad \nabla \mathcal{P} \approx \frac{p_{i,j+1} - p_{i,j}}{h}, \tag{3}$$

depending on whether the pipe is oriented horizontally or vertically. Assuming that the fluid is incompressible, the fluxes Q converging on the (i,j)th node must sum to zero; combining (2) and the approximation (3) leads to a linear equation for each unknown $p_{i,j}$:

$$\begin{aligned}(R^v_{i,j})^4(p_{i,j+1} - p_{i,j}) - (R^v_{i,j-1})^4(p_{i,j} - p_{i,j-1}) \\ + (R^h_{i,j})^4(p_{i+1,j} - p_{i,j}) - (R^h_{i-1,j})^4(p_{i,j} - p_{i-1,j}) = 0.\end{aligned} \tag{4}$$

We impose Dirichlet boundary conditions on the top and bottom: $p_{i,n} = p_t$ and $p_{i,0} = p_b$, with p_b, p_t defining the pressure drop $p_b - p_t > 0$, as discussed previously in this subsection, and periodic boundary conditions on the sides. To be more precise, the $(0, j)$th and (m, j)th nodes are connected, with the consequence that the linear equations for $p_{0,j}$ and $p_{m,j}$ (with $j = 1, \ldots, n-1$) vary from (4). For example, the linear equation for $p_{0,j}$ instead becomes

$$\begin{aligned}(R^v_{0,j})^4(p_{0,j+1} - p_{0,j}) - (R^v_{0,j-1})^4(p_{0,j} - p_{0,j-1}) \\ + (R^h_{0,j})^4(p_{1,j} - p_{0,j}) - (R^h_{m,j})^4(p_{0,j} - p_{m,j}) = 0.\end{aligned} \tag{5}$$

Let $Q_{i,j}$ be the flux through the vertical pipe between the (i, j)th and $(i, j+1)$th nodes. In view of the upward flow through the random pipe network, Zhu et al. [45] define the total flux $\overline{Q}$ as the sum of the fluxes through the topmost row of vertical pipes in the network:

$$\overline{Q} = \sum_{i=0}^{m} Q_{i,n-1} = -\frac{\pi}{8\mu} \sum_{i=0}^{m} (R^v_{i,n-1})^4 \frac{p_t - p_{i,n-1}}{h}\,. \tag{6}$$

On the other hand, when the network is viewed instead as a model of a porous medium, the average velocity $\overline{U}$ depends linearly on the pressure drop $(p_t - p_b)/D$,

$$\overline{U} = -\frac{k}{\mu} \frac{p_t - p_b}{D}\,, \tag{7}$$

where k is the effective fluid permeability in the vertical direction and μ is the fluid viscosity. The usual definition of flux means that $\overline{U}$ and $\overline{Q}$ are linearly related by the cross-sectional area through which the flow occurs,

$$\overline{U} = \frac{\overline{Q}}{Lh}\,. \tag{8}$$

Substituting (6) and (7) into (8), and solving for k, leads to an equation for k depending on the model parameters and the solution of the linear system of equations (4):

$$k = \frac{\pi D}{8Lh^2} \sum_{i=0}^{m} (R^v_{i,n-1})^4 \frac{p_t - p_{i,n-1}}{p_t - p_b}\,. \tag{9}$$

Indeed, (9) is the effective permeability of the network, and is the key quantity of interest in the model of [45] for the effective fluid permeability of young sea ice.

1.2. Void bounds for fluid transport in sea ice. In this section, we discuss rigorous bounds for the fluid permeability of sea ice, derived in [14, 42], as the basis for our new bounds in the case of a bimodal inclusion size distribution. In order to do so, we first consider the formulation and definition of the effective fluid permeability tensor k of a random porous medium. Then we will define the trapping constant γ, since there is a rigorous bound on the effective permeability in terms of this related, homogenized parameter which also characterizes the random porous medium. We will also compute exactly the trapping constant for a parallel, circular cylinder geometry, which is relevant to our bounds. In our formulation we will emphasize the *multiscale* nature of the homogenization problem that one faces in this geophysical context of fluid transport through sea ice.

We are interested in sea ice as a porous medium for a given temperature T and salinity S, which determine the brine volume fraction ϕ [30, 40, 43, 44]. Within a given vertical depth range in a sea ice sheet, perhaps up to tens of centimeters or so, the microstructural characteristics can be quite uniform over many meters horizontally. In such layers the porous brine microstructure is statistically homogeneous. However, we are also interested in how the bulk properties of the ice vary with depth, where variations in temperature and salinity, as well as possibly ice type and age, affect brine microstructural features and transport properties. We think of the submillimeter scale set by the porous microstructure of the ice as the "fast" scale, and the much larger scale variations in the temperature and salinity, and thus in the bulk properties, on the order of tens of centimeters to meters, as the "slow" scale.

Consider a random porous medium occupying a region $\mathcal{V} \subset \mathbb{R}^d$ of volume $V = |\mathcal{V}|$, partitioned into two subdomains: the void phase $\mathcal{V}_1 \subset \mathcal{V}$, and solid phase $\mathcal{V}_2 \subset \mathcal{V}$. We will be interested in the infinite volume limit. Let (Ω, P) be a probability space characterizing the pore microstructure, where Ω is the set of realizations ω of the random medium and P is a probability measure on Ω. For any realization $\omega \in \Omega$, let $\chi(\mathbf{x}, \omega)$ be the characteristic or indicator function of the void or brine phase $\mathcal{V}_1$,

$$\chi(\mathbf{x}, \omega) = \begin{cases} 1, & \mathbf{x} \in \mathcal{V}_1\,, \\ 0, & \mathbf{x} \in \mathcal{V}_2\,. \end{cases} \tag{10}$$

We first assume that $\chi(\mathbf{x}, \omega)$ is a stationary random field such that P has translation invariant statistics, corresponding to the infinite medium in all of $\mathbb{R}^d$. Then the medium is statistically homogeneous, and satisfies an *ergodic hypothesis*, where ensemble averaging over realizations $\omega \in \Omega$ is equivalent to an infinite volume limit $V \to \infty$ of an integral average over $\mathcal{V} \subset \mathbb{R}^3$, denoted by $\langle \cdot \rangle$ [41]. This and related limits have been shown to exist and to be equal to the ensemble average in some situations, thus establishing the ergodic hypothesis [10, 16].

For many porous media [14, 41], there is typically a characteristic, microscopic length scale ℓ associated with the medium, such as the "typical" size of the brine inclusions in sea ice. For example, the scale over which the two point correlation function for the void phase varies is a good measure of this length. It is small compared to a typical macroscopic length scale L, where by L here we mean sample size or thickness of a statistically homogeneous layer, on the order of $\sqrt[3]{V}$ in three dimensions. Then the parameter $\epsilon = \ell/L$ is small, and one is interested in obtaining the effective fluid transport behavior in the limit as $\epsilon \to 0$. To obtain such information, the method of *two-scale homogenization* or *two-scale convergence* [1, 2, 16, 20, 36, 37, 39, 41] has been developed in various forms, based on the identification of two scales: a slow scale $\mathbf{x}$ and a fast scale $\mathbf{y} = \mathbf{x}/\epsilon$.

The velocity and pressure fields in the pore space, $\mathbf{u}^\epsilon(\mathbf{x})$ and $p^\epsilon(\mathbf{x})$, for $\mathbf{x} \in \mathcal{V}_1$, are assumed to depend on these two scales $\mathbf{x}$ and $\mathbf{y}$. The idea is to *average*, or *homogenize* over the fast microstructural scale $\mathbf{y}$, leading to a simpler equation in the slow variable $\mathbf{x}$ describing the overall behavior of the flow, namely, Darcy's law. Variations of average microstructural properties on the slower $\mathbf{x}$ scale can then be incorporated through dependence of the effective permeability tensor on $\mathbf{x}$. For example, the bulk properties of sea ice in situ typically vary with depth, particularly when there is a large temperature gradient between the top and bottom of the sea ice layer.

The slow (creeping) flow of a viscous fluid with velocity field $\mathbf{u}^\epsilon(\mathbf{x})$ and pressure field $p^\epsilon(\mathbf{x})$ in the void phase $\mathcal{V}_1$ is governed by the Stokes equations,

$$\nabla p^\epsilon = \mu \Delta \mathbf{u}^\epsilon, \;\; \mathbf{x} \in \mathcal{V}_1, \quad \nabla \cdot \mathbf{u}^\epsilon = 0, \;\; \mathbf{x} \in \mathcal{V}_1, \quad \mathbf{u}^\epsilon(\mathbf{x}) = \mathbf{0}, \;\; \mathbf{x} \in \partial \mathcal{V}_1. \tag{11}$$

A force acting on the medium such as gravity can be incorporated into p^ϵ. From left to right in (11), we have the steady state fluid momentum equation in the zero Reynolds number limit, the incompressibility condition, and the no-slip boundary condition on the pore surface. The macroscopic equations can be derived through a two-scale expansion [1, 2, 16, 20, 36, 37, 39, 41]

$$\mathbf{u}^\epsilon(\mathbf{x}) = \epsilon^2 \mathbf{u}_0(\mathbf{x}, \mathbf{y}) + \epsilon^3 \mathbf{u}_1(\mathbf{x}, \mathbf{y}) + \cdots, \tag{12}$$

$$p^\epsilon(\mathbf{x}) = p_0(\mathbf{x}, \mathbf{y}) + \epsilon p_1(\mathbf{x}, \mathbf{y}) + \cdots. \tag{13}$$

Note that the leading term in the velocity expansion is $O(\epsilon^2)$, while the leading term in the pressure expansion is $O(1)$. This physical effect was handled in [1, 2] analytically by scaling the viscosity of the fluid by $O(\epsilon^2)$, which balances the friction of the fluid from the no-slip boundary condition on the solid boundaries of the pores. Substitution of the two-scale expansion into the Stokes equations yields systems of equations involving both $\mathbf{x}$ and $\mathbf{y}$ derivatives.

The leading order system is analyzed by considering a second order tensor velocity field $\mathsf{w}(\mathbf{y})$ and a vector pressure field $\boldsymbol{\pi}(\mathbf{y})$ [41], both varying on the fast scale, which satisfy

$$\Delta \mathsf{w} = \nabla \boldsymbol{\pi} - \mathsf{I}, \quad \mathbf{y} \in \mathcal{V}_1, \qquad \nabla \cdot \mathsf{w} = 0, \quad \mathbf{y} \in \mathcal{V}_1, \qquad \mathsf{w} = 0, \quad \mathbf{y} \in \partial \mathcal{V}_1, \tag{14}$$

where I is the identity matrix, and both w and $\boldsymbol{\pi}$ are extended to all of $\mathcal{V}$ by taking their values in the solid phase $\mathcal{V}_2$ (ice) to be 0. In these equations, the (i,j)th component of w is the jth component of the velocity due to a unit pressure gradient in the ith direction, and π_j is the jth component of the associated scaled pressure. By averaging the leading order term of the velocity $\mathbf{u}_0$ over $\mathbf{y}$, we obtain the macroscopic equations governing the flow through the porous medium,

$$\mathbf{u}(\mathbf{x}) = -\frac{1}{\mu}\, \mathsf{k} \cdot \nabla p(\mathbf{x}), \quad \mathbf{x} \in \mathcal{V}, \tag{15}$$

$$\nabla \cdot \mathbf{u} = 0, \quad \mathbf{x} \in \mathcal{V}, \tag{16}$$

where $p(\mathbf{x}) = p_0(\mathbf{x})$ and

$$\mathsf{k} = \langle \mathsf{w} \rangle \tag{17}$$

is the effective fluid permeability tensor. Equation (15) is known as Darcy's law, and (16) is the macroscopic incompressibility condition. These macroscopic equations were obtained in [1, 2] for periodic media through an appropriate limit as $\epsilon \to 0$. We shall be interested in the permeability in the vertical direction $k := k_{zz}$, in units of m^2.

We now consider the steady-state trapping problem with perfectly absorbing traps [14, 41, 42], where diffusion of a passive tracer occurs in $\mathcal{V}_1$ and trapping occurs on the surface of the solid phase $\mathcal{V}_2$ (or the boundary of the pore space $\partial \mathcal{V}_1$). The tracer concentration field $c(\mathbf{x})$ is governed by

$$\mathcal{D} \Delta c(\mathbf{x}) = -G, \ \mathbf{x} \in \mathcal{V}_1, \qquad c = 0, \ \mathbf{x} \in \partial \mathcal{V}_1, \tag{18}$$

with diffusion coefficient $\mathcal{D}$ and generation rate per unit trap-free volume G. For an ergodic medium, two-scale homogenization [1, 41] shows that γ obeys the first

order rate equation $G = \gamma \mathcal{D} C$, with average concentration $C = \langle c(\mathbf{x}) \rangle$, and trapping constant defined via

$$\gamma^{-1} = \langle u \rangle = \lim_{V \to \infty} \left(\frac{1}{V} \int_{\mathcal{V}} u(\mathbf{x}) d\mathbf{x} \right), \tag{19}$$

with volume $V = |\mathcal{V}|$, and scaled concentration field $c(\mathbf{x}) = \mathcal{D}^{-1} G u(\mathbf{x})$ solving

$$\Delta u(\mathbf{x}) = -1, \ \mathbf{x} \in \mathcal{V}_1, \quad u(\mathbf{x}) = 0, \ \mathbf{x} \in \partial \mathcal{V}_1. \tag{20}$$

For dimensions $d = 2, 3$, γ^{-1} has units of length squared. A key result that we use is a bound on the permeability in terms of the trapping constant, as in Theorem 23.5 of [41],

$$\mathsf{k} \leq \gamma^{-1} \mathsf{I}, \tag{21}$$

in the sense that $\gamma^{-1}\mathsf{I} - \mathsf{k}$ is always a positive semidefinite matrix, with equality in the case of transport through parallel channels of constant cross-section.

Consider now the case of parallel circular cylinders, with radii given by a random distribution R_I, and define the nth moment as

$$\langle R_I^n \rangle = \frac{1}{\rho} \sum_{k=1}^{\infty} \rho_k R_{I_k}^n, \tag{22}$$

where ρ_k is the number density of the kth size R_{I_k}, and ρ the characteristic density. Recall now that γ is defined in terms of (19) and (20). For a given cylinder with radius r_i, the solution of (20) is

$$u(r) = \frac{1}{4}(r_i^2 - r^2). \tag{23}$$

Given the symmetry in the direction along the axis of each cylinder, we reduce to a two-dimensional model by restricting our focus to a "slice" (plane), perpendicular to each axis. Then (19) becomes a two-dimensional integral, where V has units of length squared. Substituting (23) into (19) yields

$$\begin{aligned} \gamma^{-1} &= \lim_{V \to \infty} \left(\frac{1}{V} \sum_{i=1}^{\infty} \int_0^{2\pi} \int_0^{r_i} \frac{1}{4}(r_i^2 - r^2) r dr d\theta \right) \\ &= \lim_{V \to \infty} \left(\frac{1}{V} \sum_{i=1}^{\infty} \frac{\pi r_i^4}{8} \right), \end{aligned} \tag{24}$$

where the sum is over all the cylindrical inclusions in the void space $\mathcal{V}_1$, indexed by $i \in \mathbb{N}$. In the infinite volume limit, (24) can be expressed in a form similar to (22) as a sum over k, involving the number density ρ_k:

$$\gamma^{-1} = \frac{\pi}{8} \sum_{k=1}^{\infty} \rho_k R_{I_k}^4. \tag{25}$$

The volume fraction of the inclusions we are considering can be defined as $\phi = \rho \frac{\pi^{d/2}}{\Gamma(1+d/2)} \langle R_I^d \rangle$ [32], where $\Gamma(z) = \int_0^{\infty} t^{z-1} e^{-t} dt$ is the gamma function. Here we consider $d = 2$, in which case the volume fraction is given by

$$\phi = \rho \pi \langle R_I^2 \rangle. \tag{26}$$

Solving for π in (26), and substituting into (25) yields

$$\gamma^{-1} = \frac{\phi}{8\langle R_I^2\rangle}\frac{1}{\rho}\sum_{k=1}^{\infty}\rho_k R_{I_k}^4 = \frac{\phi\langle R_I^4\rangle}{8\langle R_I^2\rangle}. \tag{27}$$

Equation (27) defines the effective trapping constant γ for the special case of diffusion occurring in parallel, circular cylinders. Recalling the discussion surrounding (21), in this special case we have

$$\mathsf{k} = \frac{\phi\langle R_I^4\rangle}{8\langle R_I^2\rangle}\mathsf{I}. \tag{28}$$

Moreover, because $\mathsf{k} \le \gamma^{-1}\mathsf{I}$ in general geometries, the upper bound

$$\mathsf{k} \le \frac{\phi\langle R_I^4\rangle}{8\langle R_I^2\rangle}\mathsf{I} \tag{29}$$

applies for general random porous media, from which it is straightforward to recover the void upper bound stated in [14, 42].

2. Previous results. In this section we recall the previous results of [13, 45].

2.1. Choice of random distribution. A random distribution which governs the choices of the radii $R_{i,j}^h, R_{i,j}^v$ of each pipe in the network is still required (alternatively, the cross-sectional areas $A_{i,j}^h, A_{i,j}^v$ of each pipe). In [27], the observed distribution for the cross-sectional area of brine inclusions in young sea ice (among other ice types) was best fit by a lognormal distribution, i.e.,

$$A = e^X, \quad f_X(x;\mu,\sigma^2) = \frac{1}{\sqrt{2\sigma^2\pi}}e^{-\frac{(x-\mu)^2}{2\sigma^2}}. \tag{30}$$

Recall that, for a lognormal random variable A, we have

$$\mathrm{E}[A] = e^{\mu+\frac{\sigma^2}{2}} \quad \text{and} \quad \mathrm{Var}[A] = (e^{\sigma^2}-1)e^{2\mu+\sigma^2}. \tag{31}$$

In [14] it was found that the function

$$a(\phi) = \pi(7\times 10^{-5} + 1.6\times 10^{-4}\phi)^2 \text{ m}^2 \tag{32}$$

approximated the dependence of the mean cross-sectional areas on ϕ observed by [27].

Indeed, in [45], the cross-sectional areas of each pipe are lognormally distributed, with expectation given by (32),

$$\mathrm{E}[A] = a(\phi). \tag{33}$$

A short calculation, after substituting (31) and (32) into (33), yields

$$\mu + \frac{\sigma^2}{2} = \ln a(\phi). \tag{34}$$

The parameter model considered in [45] for the lognormal random variable A is then as follows: let σ be a free parameter, and let $\mu = \ln a(\phi) - \frac{\sigma^2}{2}$.

2.2. Upper bound on the fluid permeability. As discussed in subsection 1.1 for random porous media, the upper bound on the effective permeability tensor k is given by the inverse of the trapping constant γ^{-1}, in the case of parallel cylinders of random radii.

In the random pipe network model, we are interested in the effective permeability in the vertical direction, denoted as in subsection 1.2 by $k := k_{zz}$. As a discrete model for the general random medium considered in (29), we will use the general bound

$$k \leq \gamma^{-1} = \frac{\phi \langle R_I^4 \rangle}{8 \langle R_I^2 \rangle} \tag{35}$$

for the network model vertical permeability. Recall that (35) was derived in the context of circular, parallel cylinders, in which case we can reformulate (35) as

$$k \leq \frac{\phi \langle A_I^2 \rangle}{8\pi \langle A_I \rangle}\,. \tag{36}$$

For the random pipe network model of [45], we have a specific random distribution in mind—the lognormal distribution. Recalling (30), the nth moment of a lognormal random variable A with parameters (μ, σ^2) is given by

$$\begin{aligned} \langle A^n \rangle &= \mathrm{E}[A^n] = \mathrm{E}[\exp(nX)] \\ &= \int_{-\infty}^{\infty} e^{nx} (2\pi\sigma^2)^{-1/2} \exp[-(x-\mu)^2/(2\sigma^2)] dx \\ &= \int_{-\infty}^{\infty} (2\pi\sigma^2)^{-1/2} \exp[nx - (x-\mu)^2/(2\sigma^2)] dx. \end{aligned} \tag{37}$$

Some algebra yields

$$nx - \frac{(x-\mu)^2}{2\sigma^2} = -\frac{\left(x - (\mu + n\sigma^2)\right)^2}{2\sigma^2} + \frac{n(2\mu + n\sigma^2)}{2}. \tag{38}$$

Let $\mu' = \mu + n\sigma^2$; then combining (37) and (38) yields

$$\begin{aligned} \langle A^n \rangle &= \int_{-\infty}^{\infty} (2\pi\sigma^2)^{-1/2} \exp\left[-\frac{(x-\mu')^2}{2\sigma^2}\right] \exp\left[\frac{n(2\mu + n\sigma^2)}{2}\right] dx \\ &= \exp\left[\frac{n(2\mu + n\sigma^2)}{2}\right] \underbrace{\int_{-\infty}^{\infty} (2\pi\sigma^2)^{-1/2} \exp\left[-\frac{(x-\mu')^2}{2\sigma^2}\right] dx}_{=1} \\ &= \exp\left[\frac{n(2\mu + n\sigma^2)}{2}\right]. \end{aligned} \tag{39}$$

Based on (36), we need to compute $\langle A^n \rangle$ for $n = 1, 2$. For $n = 1$, $\langle A \rangle = \mathrm{E}[A]$ is given in (33),

$$\langle A \rangle = a(\phi), \tag{40}$$

while for $n = 2$,

$$\begin{aligned} \langle A^2 \rangle &= \exp\left[2\mu + 2\sigma^2\right] = \exp\left[2\mu + \sigma^2\right] e^{\sigma^2} = \left(\exp\left[\mu + \frac{\sigma^2}{2}\right]\right)^2 e^{\sigma^2} \\ &= (a(\phi))^2 e^{\sigma^2}. \end{aligned} \tag{41}$$

Thus, combining (40) and (41) with (36) yields

$$k(\phi) \leq \frac{\phi}{8\pi} a(\phi) e^{\sigma^2}, \tag{42}$$

which is precisely the upper bound stated in [13, 45].

2.3. Numerical results. Two figures of [13, 45], showing the key results of the original random pipe network model, are reconstructed in Figure 2. Note that the second of the two figures, Figure 2(b), shows the results of a slight modification of the model, to be described in this subsection.

Indeed, while the results of the original model, shown in Figure 2(a), agree well with the laboratory data of [9] for large ϕ, they disagree with the lab data for small ϕ by more than an order of magnitude. Note that the logarithm of the lab data decreases somewhat linearly for large ϕ, and drops precipitously as $\phi \to 0.05^+$. Physically, this precipitous drop can be understood in terms of the "Rule of Fives" [11], whereby columnar sea ice undergoes a temperature-driven transition from an impermeable porous medium to one where the pores have connected to form channels through which fluid can flow at around $\phi = 0.05$ (when temperature $T = -5^o$C and bulk salinity $S = 5$ ppt). Keeping in mind the Rule of Fives, the random pipe network formulation, and the discrepancy between the numerical results and the data shown in Figure 2(a), leads one to the conclusion that a means by which the network can become largely disconnected as $\phi \to 0.05^+$ must be introduced.

In [13], two additional parameters were introduced to allow for the requisite disconnection to occur: we will refer to these as "disconnection probabilities," and denote them as $p_h \in [0, 1]$, the probability that a horizontal pipe will be "broken" (removed), and $p_v \in [0, 1]$, the probability that a vertical pipe will be broken. Conceptually, nonzero (p_h, p_v) will cause the random pipe network to have "gaps" through which fluid cannot flow. In terms of the model discussed in subsection 1.1, this impedance of flow is achieved by drawing a sample of random numbers $U^h_{i,j}$ and $U^v_{i,j}$ from a uniform random variable $U = \text{unif}(0, 1)$, with $i, j = 0, 1, \ldots, N + 1$, and then setting $R^\alpha_{i,j} = 0$ if $U^\alpha_{i,j} < p_\alpha$ for $\alpha = h, v$. The choice of (p_h, p_v) in [13] varied with volume fraction ϕ, so that the network was largely disconnected as $\phi \to 0.05^+$, with the result reconstructed in Figure 2(b) showing excellent agreement with the laboratory data of [9].

Although the random pipe network model summarized herein is two-dimensional and reflects only the basic features of sea ice microstructure, the results [13, 45] of numerical simulations, reconstructed in Figure 2, lie well within void bounds and agree with laboratory data, particularly with the disconnection probabilities p_h and p_v.

3. Random pipe model for sea ice with entrained EPS. Consider now a model for the effective permeability k of a vertical slab of sea ice with entrained EPS (e.g., due to the presence of algae). As in subsections 1.2, 2.1, and 2.3, we regard our random network as a simplified model of the pore space of a statistically homogeneous vertical slab of ice (in equilibrium), and are interested in the vertical effective permeability of the network, as a model for the vertical effective permeability of the ice.

Recall from section 1, however, that there are key differences between young sea ice with and without entrained EPS, as observed in [23]: increased tortuosity, increased volume fraction, increased salt retention, and a net drop in fluid permeability.

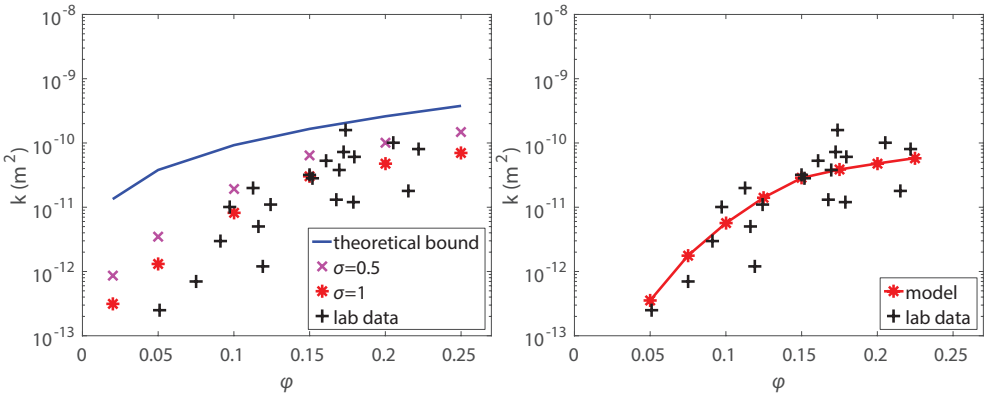

(a) Reconstruction of Fig. 2 from [45]. (b) Reconstruction of Fig. 4(b) from [13].

FIG. 2. *Previous results (see subsection* 2.3*): Plots of* k *(in* m^2*) versus* ϕ*, in* (b) *with and in* (a) *without effects of percolation, respectively. Note that* $N = 1024$*,* $p_b = 1$*,* $p_t = 0$*,* $h = \sqrt{2a(\phi)/\phi}$*, and* $L = D = hN$ *(for details, see* [45]*). As shown in* (a)*, simulations with* $\sigma = 0.5$ *and* $\sigma = 1.0$ *are both considered, while in* (b) $\sigma = 1.0$*. Note that the laboratory data of* [9] *and axes in both figures are identical.*

In the context of our random pipe model, some of these key differences are well reflected, while others are not. Although increased geometric complexity of individual pores is not represented (due to the choice of circular pipes), we expect that the new choice of random distribution (44)—which permits a wider range of pipe sizes—contributes to the modeling of increased tortuosity. Furthermore, we will consider similar volume fractions as in [45], in order to compare with the results of the original model. Moreover, since we consider an equilibrium model, we do not take into account salinity or temperature. Lastly, the effective permeability is the variable to be modeled, and so the observed net drop is not presumed to be known a priori.

Expanding on this last point (the drop in effective permeability), while specific data for fluid permeability were not presented in [23], the text made clear that the decrease in fluid permeability was by at most an order of magnitude.

It will be useful going forward to discuss (1) the data of [23] and (2) our data processing and assumptions.

1. From [23], the data were collected as follows: (i) the diatom *Melosira arctica* var. *krembsii* was isolated from the bottom of sea ice in the Chukchi Sea near Barrow, Alaska; (ii) cells were cultured and reached significant biomass and EPS production; (iii) artifical sea ice was grown in 13–L tanks at $-10°$C from saline solution containing *Melosira* EPS; and (iv) photomicrographic measurements of $n = 234$ brine inclusions from the artificially grown sea ice were conducted at $-10°$C, in particular measurements of pore perimeter versus maximum inclusion length under high magnification.
2. In order to use the data of [23] in our random pipe network (to be discussed shortly, following this list), we need to assume that the brine cross-sections are circular, and calculate the area of the assumed circular cross-sections from their measured perimeters, via $A = P^2/(4\pi)$. The validity of this assumption is unfortunately questionable, but is an artifact of the model used. Indeed, in [23] it is observed that the pore space in artificial sea ice grown with *Melosira* EPS is more geometrically complex than in controls (artificial and natural sea

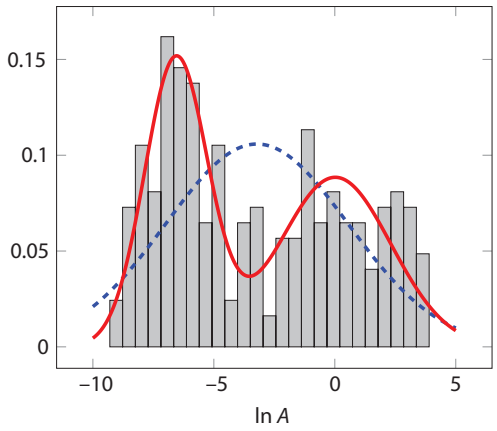

FIG. 3. *Bimodal-lognormal distribution for the cross sectional areas of the brine inclusions in EPS-laden sea ice, using data from* [23]. *The histogram of* $\log(A)$ *for observed values of cross-sectional area* A *of young sea ice with entrained EPS (scaled with the sum of box areas equal to unity) is shown in gray. Superimposed are the best fit probability density functions (PDF), with the normal PDF (dashed, in blue) corresponding to the classical lognormal distribution in* [27], *and the new bimodal PDF (solid, in red). (Figure is in color online.)*

ice grown without *Melosira* EPS), i.e., not circular. Nonetheless, we proceed with the calculation as these are the only data available, and acknowledge as important future work the need to (i) better quantify the geometrical complexity experimentally, and (ii) better model this complexity.

With these details clarified, let us now discuss our new model. From a modeling perspective, the components are largely the same as described in subsection 1.1 and section 2. We consider a vertical slab of young sea ice (with entrained EPS) at a given equilibrium state, and model the pore space of the ice as a square lattice (1) with circular pipes (cf. Figure 1) connecting a given node (i, j) to its nearest neighbors $\{(i \pm 1, j), (i, j \pm 1)\}$. Assuming classic Poiseuille flow, approximation by finite differences, and incompressibility, we derive the linear system (4). Defining the total flux, average velocity, and their linear relationship (6)–(8), and solving for k leads to the definition for the effective permeability (9) of the network. These components constitute our model for the effective permeability of a vertical slab of young sea ice with entrained EPS. At this point, however, we must consider the choice of cross-sectional area distribution and parameters.

It was observed in [27] that a lognormal distribution (30) models well the observed data on brine inclusion cross-sectional area A in young sea ice. In the case of young sea ice with entrained EPS, we consider the data of [23], transformed into measurements of area via $A = P^2/(4\pi)$; see the histogram in Figure 3. Indeed, based on the histogram, we hypothesized that a more accurate model for $\log A$ might be given by a *bimodal* rather than a *unimodal* distribution.

There are several statistical measures of bimodality. Freeman and Dale [8] investigated three different measures, and found utility in the "Bimodality Coefficient" (BC) [38]. The BC does not assume a specific underlying distribution, and is based on an empirical relationship between bimodality and the centered third and fourth moments (skewness and excess kurtosis, respectively) of a distribution [8]. The computation of the BC is straightforward [31], requiring only the sample size n, the skewness m_3 of

the observed distribution, and its excess kurtosis m_4:

$$\text{BC} = \frac{m_3^2 + 1}{m_4 + \frac{3(n-1)^2}{(n-2)(n-3)}}. \tag{43}$$

The BC is between 0 and 1; values larger than $5/9 \approx 0.555$ suggest bimodality, while values smaller than 5/9 suggest unimodality. For the data set in [23], with sample size $n = 234$, we find that BC ≈ 0.61, which does indeed suggest bimodality of the underlying distribution.

With BC ≈ 0.61 in (43) supporting the hypothesis of a bimodal distribution, we now postulate the precise form for a model of the distribution of the pipe cross-sectional areas. A natural generalization of the classical lognormal distribution (30), which can incorporate bimodality given certain parameters, involves a mixture of two normal distributions:

$$A = e^Y, \quad f_Y(x; \mu_1, \mu_2, \sigma_1^2, \sigma_2^2) = p f_X(x; \mu_1, \sigma_1^2) + (1-p) f_X(x; \mu_2, \sigma_2^2). \tag{44}$$

Indeed, computing a maximum-likelihood estimate for the parameters of (44), applied to the transformed data of [23], yields

$$(p, \mu_1, \mu_2, \sigma_1, \sigma_2) = (0.48, -6.56, 0.02, 1.30, 2.30). \tag{45}$$

In Figure 3, we have plotted the graph of f_Y in (44) with the parameters in (45), clearly showing the bimodality of the probability density function f_Y. (Quantitatively, we can also apply the modality theorem of [35] to show bimodality.)

While this new *bimodal–lognormal* distribution (44) gives a good approximation between our random pipe model and existing experimental data (discussed shortly, in subsection 3.2), it might be possible to suggest a more accurate approximation if additional data will become available.

3.1. Upper bound on fluid permeability in EPS-laden sea ice. In this subsection, we explicitly calculate the new void bound (36) (cf. (42)), i.e., the upper bound on fluid permeability k for our new model using the bimodal–lognormal distribution (44). Indeed, the moments of $A = e^Y$ can be computed explicitly. The first step is to observe that

$$\langle A^n \rangle = \text{E}[A^n] = \text{E}[\exp(nY)] = \int_{-\infty}^{\infty} e^{ny} \sum_{i=1}^{2} w_i f(y; \mu_i, \sigma_i^2) dy, \tag{46}$$

where $w_1 = p$, $w_2 = 1 - p$, and $f(y; \mu, \sigma^2) = (2\pi\sigma^2)^{-1/2} \exp[-(y-\mu)^2/(2\sigma^2)]$. The remainder of the calculation follows subsection 2.2, (37)–(41):

$$\langle A^n \rangle = p \exp\left[\frac{n(2\mu_1 + n\sigma_1^2)}{2}\right] + (1-p) \exp\left[\frac{n(2\mu_2 + n\sigma_2^2)}{2}\right]. \tag{47}$$

Then, combining (36) and (47) with $n = 1, 2$ yields

$$k \leq \frac{\phi\left(p \exp\left[2\mu_1 + 2\sigma_1^2\right] + (1-p) \exp\left[2\mu_2 + 2\sigma_2^2\right]\right)}{8\pi\left(p \exp\left[\frac{2\mu_1 + \sigma_1^2}{2}\right] + (1-p) \exp\left[\frac{2\mu_2 + \sigma_2^2}{2}\right]\right)}. \tag{48}$$

Including the parameters discussed in subsection 3.2 simplifies (48) considerably (see (51)) .

TABLE 1
The choice of parameters (p_h, p_v) used in new simulations (Figure 4), to model the percolation transition [11] *as $\phi \to 0.05^+$, similar to* [13].

ϕ	p_h	p_v	ϕ	p_h	p_v
0.05	0.45	0.375	0.15	0	0
0.075	0.35	0.3	0.175	0	0
0.10	0.25	0.2	0.20	0	0
0.125	0.15	0.1	0.225	0	0

3.2. Numerical results. We now discuss parameter selection, the simplified form of the void upper bound, numerical simulations of the new random pipe network model, and computational considerations.

Recalling from section 3 (Figure 3 and (44) and (45)), the data of [23] were measured from photomicrographs of $n = 234$ brine inclusions at $-10°$C. The data therefore give a quantitative understanding of the brine inclusions in one sample of sea ice with entrained EPS, at some given brine volume fraction $0 < \phi < 1$. In order to compare and contrast with the previous results [13] and data [9], however, we wish to have a series of samples, with varying brine volume fraction ϕ, in particular $\phi \to 0.05^+$. In the absence of conclusive data to make mathematical modeling decisions with regard to the parameters, we proceed as follows.

As before (subsections 2.1 and 2.3), we require $\mathrm{E}[A] = a(\phi)$, where $a(\phi)$ is given by (32), but A is given by the new bimodal distribution (44). As ϕ varies, we suppose that $\epsilon = \frac{\mu_2 - \mu_1}{2}$ is fixed. Additionally, we let $\sigma = \sigma_1 = \sigma_2$ be a free parameter, let $\mu_1 = \ln a(\phi) - \frac{\sigma^2}{2} - \epsilon$, and let $\mu_2 = \ln a(\phi) - \frac{\sigma^2}{2} + \epsilon$. In summary, we have

$$\begin{aligned} &\epsilon = \tfrac{\mu_2 - \mu_1}{2}, && \sigma = \sigma_1 = \sigma_2 \text{ is a free parameter,} \\ &\mu_1 = \ln a(\phi) - \tfrac{\sigma^2}{2} - \epsilon, && \mu_2 = \ln a(\phi) - \tfrac{\sigma^2}{2} + \epsilon. \end{aligned} \tag{49}$$

Given the parameters (49), and the requirement that $\mathrm{E}[A] = a(\phi)$, a straightforward but tedious calculation begins by substituting (49) into (47) (with $n = 1$), and concludes with the realization that p is, in fact, a dependent parameter,

$$p(\epsilon) = \frac{1}{1 + e^{-\epsilon}}\,. \tag{50}$$

We also incorporate the disconnection probabilities (p_h, p_v), which are chosen as in [13], so that the network is largely disconnected as $\phi \to 0.05^+$. The specific parameters used are given in Table 1. To both reiterate and expand on the discussion of (p_h, p_v) from subsection 2.3, our choices for p_h and p_v (i) act as a model of the percolation transition [11] observed in sea ice (the aforementioned Rule of Fives), (ii) were observed as necessary in [13], and (iii) are similar to (but not the same as) the parameters used in [13].

With the choice of parameters as in (49) and (50), (48) reduces to

$$k(\phi) \le (2\cosh\epsilon - 1)\frac{\phi}{8\pi} a(\phi) e^{\sigma^2}. \tag{51}$$

Assuming $\mu_2 \ge \mu_1$, then $\epsilon \ge 0$. When $\epsilon = 0$, the separation $\mu_2 - \mu_1 = 0$, and the underlying probability distribution is the classical lognormal distribution, as in the

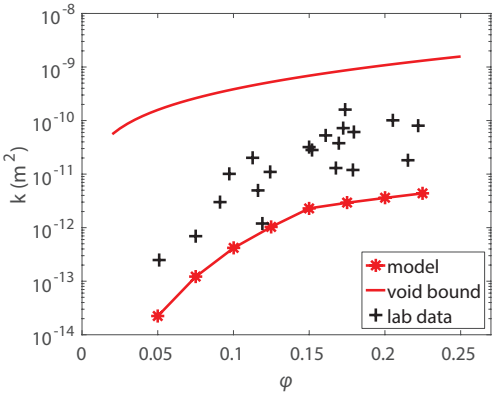

FIG. 4. *Model results for young sea ice with entrained EPS: Plot of k (in m^2) versus ϕ, with nonzero disconnection probabilities (p_h, p_v) for $\phi < 0.15$ (Table 1), modeling the percolation transition* [11] *as $\phi \to 0.05^+$. Parameters: $m = n = 1024$, $\sigma^2 = 1$. The solid-starred line represents the numerical results, computed for the volume fractions $\phi = 0.05, 0.075, 0.1, 0.125, 0.15, 0.175, 0.2, 0.225$; the solid line represents the upper bound* (51) *with $\epsilon = 1.6$; while the lab data* [9] *is for young sea ice* without *EPS.*

original model [45] (subsections 1.1, 2.1, and 2.3). In this case, (51) reduces to (42), reinforcing that our model is an extension of the existing model.

As discussed at the start of section 3, the observed drop in fluid permeability [23] of young sea ice with entrained EPS versus EPS-free ice was by at most an order of magnitude. When we choose $\epsilon = 3.3$, as suggested by (45) and (49), we see too severe a drop in k—by three orders of magnitude instead of one. Choosing instead $\epsilon = 1.6$, we see by comparing Figure 2(b) and Figure 4 that the drop in fluid permeability is in much better agreement, with only a slight overestimate when $\phi < 0.15$. The severe drop by the natural choice of $\epsilon = 3.3$ may be due to a lack of precision in the original data, the lack of geometric information in the data, or the lack of geometric complexity in the model, while the slight overestimate when $\epsilon = 1.6$ and $\phi < 0.15$ may be due to the choices for (p_h, p_v)—which were not quite the same as the original numerical simulations reconstructed in Figure 2(b) (see Table 1).

Considering now the new, rigorous upper bound (51), when $\epsilon > 0$ we have $2\cosh\epsilon - 1 > 1$, so the upper bound (51) is similar to (42), up to a multiplicative constant $C > 1$. With the choice of $\epsilon = 1.6$ as discussed above, $C = 2\cosh\epsilon - 1 \approx 4.15$, which means that our void bound for the new bimodal–lognormal distribution is approximately four times larger than the void bound for the original lognormal distribution—opposite the previously observed and now numerically simulated drop in fluid permeability k. Ideally, we would have a somewhat tight (if not optimal) upper bound, which suggests the need for additional analysis.

Recalling the discussion in the text surrounding (21) and (28), (51) becomes an equality in a parallel-cylinder geometry—in this sense, it is an *anisotropic* upper bound. Indeed, in the parallel-cylinder geometry, fluid will easily flow through large pipes, which are made more readily available by the new bimodal–lognormal distribution (cf. Figure 3). On the other hand, the numerical simulations summarized in Figure 4 involve a random, isotropic pipe network, in which the fluid does not flow in a preferred direction. This disagreement—between an anisotropic, parallel-cylinder geometry, and an isotropic pipe network—explains the apparent disparity between the rigorous upper bound (51) and numerical simulations.

While this type of anisotropic upper bound is sensible for fluid flow in classical, columnar sea ice (as summarized in subsection 2.2) due to the anistropic geometry of its microstructure, the geometry of ice with entrained EPS that we have seen is typically more isotropic. We therefore expect that an *isotropic* bound, as in [3], may be more relevant, and in particular may reduce the apparent disparity between numerical simulations and upper bounds. While the analysis of isotropic bounds is beyond the scope of the present work, this is an exciting future direction that we are currently pursuing.

When the linear system (4) and (5) is constructed using the original, classical lognormal distribution for the underlying coefficients (as in subsections 1.1, 2.1, and 2.3), and $N = 1024$, the solution time for the iterative multigrid solver of [45] (implemented in Fortran) increases rapidly with $\sigma > 1$. Increasing σ from 1.0 to 1.5, for example, increases the required number of iterations and thus the required time by several orders of magnitude. Similar timing increases arise when the classical lognormal distribution is replaced with the new bimodal–lognormal distribution. The issue is magnified by the choice of (p_h, p_v) for $\phi < 0.15$, which causes the underlying matrix to become indefinite.

These convergence issues and increases in computing times are perhaps not wholly unexpected, given the corresponding increase in variance, and thus the increasingly rough (random) coefficients involved. In lieu of augmenting the existing multigrid solver of [45] to better handle the real, symmetric, possibly indefinite linear system (4) and (5) with rough coefficients, we have instead designed a MATLAB implementation using built-in direct solvers—in particular a Cholesky solver when the matrix is positive definite, and the MA57 routine [6] when the matrix is numerically indefinite—for which convergence is not an issue.

To illustrate the increase in variance more clearly, we show in Table 2 the means and variances of the random lognormal or bimodal–lognormal distributions (denoted A_{orig} and A_{new}) used in the original and the new random pipe network models, respectively. Recall that $\mathrm{E}[A_{\text{orig}}] = \mathrm{E}[A_{\text{new}}] = a(\phi)$ (32), by assumption. The variances $\mathrm{Var}[A_{\text{orig}}]$ and $\mathrm{Var}[A_{\text{new}}]$, however, are not equal. Indeed, Table 2 shows that for all four values of ϕ we have $\mathrm{Var}[A_{\text{new}}] > \mathrm{Var}[A_{\text{orig}}]$, by around an order of magnitude. Indeed, in either case (the original or the new model), the effect of increasing the parameter ϕ is to increase the value of $a(\phi)$ and thus μ (for the original model) or (μ_1, μ_2) (for the new model). In the new model, however, the density function f_Y (44) has two peaks, each approximately the same width, and separated by a distance 2ϵ. Thus the increase in variance is expected.

Continuing, we can consider now how the model informs our understanding of the actual physical systems involved. Indeed, the graph of the bimodal–lognormal distribution in Figure 3 suggests that this drop in fluid permeability is not unexpected. Indeed, this drop should be evident from the dominance of the left bump centered on very small inclusions with cross-sections an order of magnitude smaller than, say, the mean of the classical lognormal distribution, leading to a higher probability of these *constrictive* pathways, and lowering the effective fluid transport properties of the porous medium.

4. Conclusions. While the effective fluid permeability of sea ice is a critical parameter affecting the properties of sea ice, and thus affecting polar ecosystems and global climate models, the effects of biogeochemistry on this parameter are not yet well understood. The random pipe network model presented herein is a mathematical model for the effective fluid permeability of young sea ice with entrained EPS, under

TABLE 2

The means and variances ($\mathrm{Var}[A_{orig}]$ *and* $\mathrm{Var}[A_{new}]$*) of the underlying random lognormal and bimodal–lognormal distributions used in the original and the new model, respectively, given the free parameter* $\sigma = 1.0$*. Recall that* $\mathrm{E}[A_{orig}] = \mathrm{E}[A_{new}] = a(\phi)$*, by assumption.*

ϕ	$a(\phi)$	$\mathrm{Var}[A_{\mathrm{orig}}]$	$\mathrm{Var}[A_{\mathrm{new}}]$
0.05	0.0191	0.000628	0.00376
0.10	0.0232	0.000928	0.00556
0.15	0.0278	0.00132	0.00793
0.20	0.0327	0.00184	0.0110

the simplifying assumption that the given slab of sea ice is at equilibrium. As far as we are aware, this paper presents the first work to consider a two-dimensional model of the effects of microscale biochemistry, and particularly the presence of algal exudates, on the larger scale physical properties of sea ice. We find good agreement between observations [23] and our numerical simulations, analyze this result, and discuss room for improvement in the observational data, modeling, and parameter selection.

Future work is needed to understand the effects of biology and chemistry on the properties of the sea ice. Indeed, direct improvements to this model could be achieved by studying data related to (1) observations of the average cross-sectional area of brine inclusions in young, EPS-laden sea ice, as a function of ϕ; and (2) observations of the fluid permeability of this type of ice, as a function of ϕ. We expect that an improved (tighter) upper bound might be found by considering an isotropic upper bound, as in [3], and are investigating this further. Formulating and analyzing a discrete, nonequilibrium, random pipe network model for fluid permeability of young sea ice represents an exciting new direction, which would require judicious modeling of salinity, temperature, phase change, and connectivity. A possible application of considerable importance to large-scale studies of sea ice would be to mathematically model percolation blockage in young sea ice, as studied in [33]. This type of modeling could help to explain why the presence of EPS in sea ice extends the lifetime of the ice [23].

Acknowledgments. We are grateful to the anonymous reviewers for valuable remarks and comments, which led to significant improvements in the paper and to new directions for future research.We are grateful to Christopher Krembs for providing the detailed measurements used in the new model analysis. Finally, we would like to thank the Math Climate Research Network (MCRN) for their support.

REFERENCES

[1] G. ALLAIRE, *Homogenization and two-scale convergence*, SIAM J. Math. Anal., 23 (1992), pp. 1482–1518, https://doi.org/10.1137/0523084.

[2] G. ALLAIRE, *One-phase Newtonian flow*, in Homogenization and Porous Media, U. Hornung, ed., Interdiscip. Appl. Math. 6, Springer, New York, 1997, pp. 45–76, https://doi.org/10.1007/978-1-4612-1920-0_3.

[3] J. G. BERRYMAN AND G. W. MILTON, *Normalization constraint for variational bounds on fluid permeability*, J. Chem. Phys., 83 (1985), pp. 754–760, https://doi.org/10.1063/1.449489.

[4] F. D. CARSEY, ed., *Microwave Remote Sensing of Sea Ice*, Geophysical Monograph Series 68, American Geophysical Union, Washington, DC, 1992, https://doi.org/10.1029/gm068.

[5] D. J. CAVALIERI AND C. L. PARKINSON, *Arctic sea ice variability and trends,* 1979–2010, The Cryosphere, 6 (2012), pp. 881–889, https://doi.org/10.5194/tc-6-881-2012.

[6] I. S. Duff, *MA57—a code for the solution of sparse symmetric definite and indefinite systems*, ACM Trans. Math. Software, 30 (2004), pp. 118–144, https://doi.org/10.1145/992200.992202.

[7] F. A. L. Dullien, *Porous Media: Fluid Transport and Pore Structure*, 2nd ed., Academic Press, New York, 1992, https://doi.org/10.1016/c2009-0-26184-8.

[8] J. B. Freeman and R. Dale, *Assessing bimodality to detect the presence of a dual cognitive process*, Behav. Res. Methods, 45 (2012), pp. 83–97, https://doi.org/10.3758/s13428-012-0225-x.

[9] J. Freitag, *The hydraulic properties of Arctic sea ice—Implications for the small-scale particle transport*, Ber. Polarforsch./Rep. Polar Res., 325 (1999), pp. 1–150.

[10] K. Golden and G. Papanicolaou, *Bounds for effective parameters of heterogeneous media by analytic continuation*, Comm. Math. Phys., 90 (1983), pp. 473–491, https://doi.org/10.1007/bf01216179.

[11] K. M. Golden, S. F. Ackley, and V. I. Lytle, *The percolation phase transition in sea ice*, Science, 282 (1998), pp. 2238–2241, https://doi.org/10.1126/science.282.5397.2238.

[12] K. M. Golden, D. Borup, M. Cheney, E. Cherkaeva, M. S. Dawson, K. H. Ding, A. K. Fung, D. Isaacson, S. A. Johnson, A. K. Jordan, J. A. Kong, R. Kwok, S. V. Nghiem, R. G. Onstott, J. Sylvester, D. P. Winebrenner, and I. Zabel, *Inverse electromagnetic scattering models for sea ice*, IEEE Trans. Geosci. Rem. Sens., 36 (1998), pp. 1675–1704, https://doi.org/10.1109/36.718638.

[13] K. M. Golden, H. Eicken, A. L. Heaton, J. Miner, D. J. Pringle, and J. Zhu, *Thermal evolution of permeability and microstructure in sea ice*, Geophys. Res. Lett., 34 (2007), L16501, https://doi.org/10.1029/2007gl030447.

[14] K. M. Golden, A. L. Heaton, H. Eicken, and V. I. Lytle, *Void bounds for fluid transport in sea ice*, Mech. Mater., 38 (2006), pp. 801–817, https://doi.org/10.1016/j.mechmat.2005.06.015.

[15] C. Haas, A. Pfaffling, S. Hendricks, L. Rabenstein, J.-L. Étienne, and I. Rigor, *Reduced ice thickness in Arctic transpolar drift favors rapid ice retreat*, Geophys. Res. Lett., 35 (2008), L17501, https://doi.org/10.1029/2008GL034457.

[16] U. Hornung, ed., *Homogenization and Porous Media*, Springer, New York, 1997, https://doi.org/10.1007/978-1-4612-1920-0.

[17] E. C. Hunke, W. H. Lipscomb, and A. K. Turner, *Sea-ice models for climate study: retrospective and new directions*, J. Glaciol., 56 (2010), pp. 1162–1172, https://doi.org/10.3189/002214311796406095.

[18] E. C. Hunke, D. Notz, A. K. Turner, and M. Vancoppenolle, *The multiphase physics of sea ice: a review for model developers*, The Cryosphere, 5 (2011), pp. 989–1009, https://doi.org/10.5194/tc-5-989-2011.

[19] J. D. Hyman, P. K. Smolarkiewicz, and C. L. Winter, *Heterogeneities of flow in stochastically generated porous media*, Phys. Rev. E, 86 (2012), 056701, https://doi.org/10.1103/PhysRevE.86.056701.

[20] J. B. Keller, *Darcy's law for flow in porous media and the two-space method*, in Nonlinear Partial Differential Equations in Engineering and Applied Sciences, R. L. Sternberg, A. J. Kalinowski, and J. S. Papadakis, eds., Lecture Notes in Pure and Appl. Math. 54, Dekker, New York, 1980, pp. 429–443.

[21] J. Koplik, *Creeping flow in two-dimensional networks*, J. Fluid Mech., 119 (1982), pp. 219–247, https://doi.org/10.1017/S0022112082001323.

[22] J. Koplik, C. Lin, and M. Vermette, *Conductivity and permeability from microgeometry*, J. Appl. Phys., 56 (1984), pp. 3127–3131, https://doi.org/10.1063/1.333872.

[23] C. Krembs, H. Eicken, and J. W. Deming, *Exopolymer alteration of physical properties of sea ice and implications for ice habitability and biogeochemistry in a warmer Arctic*, Proc. Natl. Acad. Sci. USA, 108 (2011), pp. 3653–3658, https://doi.org/10.1073/pnas.1100701108.

[24] D. Lubin and R. A. Massom, *Polar Remote Sensing, Volume 1: Atmosphere & Polar Oceans*, Springer Praxis Books, Springer, Berlin, 2006, https://doi.org/10.1007/3-540-30785-0.

[25] M. G. McPhee, S. F. Ackley, P. Guest, B. A. Huber, D. G. Martinson, J. H. Morison, R. D. Muench, L. Padman, and T. P. Stanton, *The Antarctic zone flux experiment*, Bull. Amer. Met. Soc., 77 (1996), pp. 1221–1232, http://journals.ametsoc.org/doi/abs/10.1175/1520-0477%281996%29077%3C1221:TAZFE%3E2.0.CO%3B2.

[26] K. M. Meiners, K. M. Golden, P. Heil, J. Lieser, R. Massom, B. Meyer, and G. D. Williams, eds., *East Antarctic Sea-Ice Physics and Ecosystem Processes*, Deep Sea Research Part II: Topical Studies in Oceanography 131, Elsevier, 2016.

[27] D. Perovich and A. Gow, *A quantitative description of sea ice inclusions*, J. Geophys. Res., C8 (1996), pp. 18327–18343, https://doi.org/10.1029/96jc01688.
[28] D. K. Perovich, T. C. Grenfell, B. Light, B. C. Elder, J. Harbeck, C. Polashenski, W. B. T. III, and C. Stelmach, *Transpolar observations of the morphological properties of Arctic sea ice*, J. Geophys. Res., 114 (2009), C00A04, https://doi.org/10.1029/2008JC004892.
[29] D. K. Perovich, W. B. T. III, and K. Ligett, *Aerial observations of the evolution of ice surface conditions during summer*, J. Geophys. Res., 107 (2002), pp. 24:1–14, https://doi.org/10.1029/2000JC000449.
[30] C. Petrich and H. Eicken, *Growth, structure, and properties of sea ice*, in Sea Ice, 2nd ed., D. N. Thomas and G. S. Dieckmann, eds., Wiley-Blackwell, West Sussex, UK, 2010, pp. 23–77, https://doi.org/10.1002/9781444317145.ch2.
[31] R. Pfister, K. A. Schwarz, M. Janczyk, R. Dale, and J. B. Freeman, *Good things peak in pairs: a note on the bimodality coefficient*, Front. Psychol., 4 (2013), pp. 700:1–4, https://doi.org/10.3389/fpsyg.2013.00700.
[32] D. C. Pham and S. Torquato, *Exactly realizable bounds on the trapping constant and permeability of porous media*, J. Appl. Phys., 97 (2005), 013535, https://doi.org/10.1063/1.1829379.
[33] C. Polashenski, K. M. Golden, D. K. Perovich, E. Skyllingstad, A. Arnsten, C. Stwertka, and N. Wright, *Percolation blockage: A process that enables melt pond formation on first year Arctic sea ice*, J. Geophys. Res. (Oceans), 122 (2017), pp. 413–440, https://doi.org/10.1002/2016JC011994.
[34] R. S. Pritchard, ed., *Sea Ice Processes and Models: Proceedings of the Arctic Ice Dynamics Joint Experiment International Commission of Snow and Ice Symposium*, University of Washington Press, Seattle, 1980.
[35] C. A. Robertson and J. G. Fryer, *Some descriptive properties of normal mixtures*, Scand. Actuar. J., 1969 (1969), pp. 137–146, https://doi.org/10.1080/03461238.1969.10404590.
[36] J. Rubinstein and S. Torquato, *Flow in random porous media: Mathematical formulation, variational principles, and rigorous bounds*, J. Fluid Mech., 206 (1989), pp. 25–46.
[37] M. Sahimi, *Flow and Transport in Porous Media and Fractured Rock*, Wiley, New York, 1995.
[38] SAS Institute Inc., *SAS/STAT* 9.1 *User's Guide*, Cary, NC, 2004.
[39] L. Tartar, *Incompressible fluid flow in a porous medium*, in Non-Homogeneous Media and Vibration Theory, E. Sanchez-Palencia, ed., Lecture Notes in Phys. 129, Springer-Verlag, Berlin, New York, 1980, pp. 368–377.
[40] D. N. Thomas and G. S. Dieckmann, eds., *Sea Ice*, 2nd ed., Wiley-Blackwell, West Sussex, UK, 2010, https://doi.org/10.1002/9781444317145.
[41] S. Torquato, *Random Heterogeneous Materials*, Interdiscip. Appl. Math. 16, Springer-Verlag, New York, 2002, https://doi.org/10.1007/978-1-4757-6355-3.
[42] S. Torquato and D. C. Pham, *Optimal bounds on the trapping constant and permeability of porous media*, Phys. Rev. Lett., 92 (2004), 255505, https://doi.org/10.1103/PhysRevLett.92.255505.
[43] N. Untersteiner, ed., *The Geophysics of Sea Ice*, NATO ASI Series (Series B: Physics), Springer, New York, 1986, https://doi.org/10.1007/978-1-4899-5352-0_1.
[44] W. F. Weeks and S. F. Ackley, *The growth, structure, and properties of sea ice*, in The Geophysics of Sea Ice, N. Untersteiner, ed., NATO ASI Series (Series B: Physics), Springer, New York, 1986, pp. 9–164, https://doi.org/10.1007/978-1-4899-5352-0_2.
[45] J. Zhu, A. Jabini, K. M. Golden, H. Eicken, and M. Morris, *A network model for fluid transport through sea ice*, Ann. Glaciol., 44 (2006), pp. 129–133, https://doi.org/10.3189/172756406781811141.